nature energy

Article

https://doi.org/10.1038/s41560-025-01902-w

Vacancy-enhanced cation ordering via magnesium doping to enable kesterite solar cells with 14.9% certified efficiency

Received: 17 November 2024

Accepted: 16 October 2025

Published online: 12 November 2025

Check for updates

Jinlin Wang[1,2,6], Fanqi Meng[3,6], Licheng Lou[1,2,6], Kang Yin[1,2,6], Xiao Xu[1], Menghan Jiao[1,2], Bowen Zhang[1,2], Yiming Li[1], Jiangjian Shi[1] ✉, Huijue Wu[1], Yanhong Luo[1,2,4], Dongmei Li[1,2,4] ✉ & Qingbo Meng[1,2,4,5] ✉

Atomic disorder is a widespread issue in multi-element crystalline materials and poses a critical challenge to the performance of $Cu_2ZnSn(S, Se)_4$ (CZTSSe) photovoltaic devices. In particular, Cu–Zn disorder is prevalent in CZTSSe due to its low formation energy, leading to the formation of high-concentration deep defects and severe charge loss. The regulation of this disorder remains challenging because of the trade-off between the thermodynamics of the disorder–order phase transition and the kinetics of atom interchange. Here we introduce additional vacancy defects at the CZTSSe surface via magnesium doping to reduce the energy barrier for atom interchange. This vacancy-assisted approach enhances the kinetics of Cu–Zn ordering, thereby reducing charge loss in the device. As a result, we achieve a power conversion efficiency of 14.9% certified by the Chinese National PV Industry Measurement and Testing Center in CZTSSe solar cells, marking an advancement in the development of emerging inorganic thin-film photovoltaics.

Entropy-driven atomic disordering is a crucial concern that impacts the precise fabrication and functional design of crystalline materials[1–4]. This issue is particularly prominent in the chalcogenide $Cu_2ZnSn(S, Se)_4$ (CZTSSe)[5–7], a promising photovoltaic material with a complex elemental composition[8–10]. CZTSSe comprises three metal cations (that is Cu, Zn and Sn) that are similar in size and share the same coordination structure within the lattice[7,11]. The disorder or reciprocal substitution between these cations triggers phase competition, bandgap fluctuations and deep energy-level defects, all of which impair the photoelectric conversion performance of CZTSSe solar cells[5,10,12,13]. Among them, the Cu–Zn disorder is particularly prevalent due to its low thermodynamic formation energy[5,14]. This disorder reduces the material's effective bandgap[15,16] and increases the concentration and charge-capturing rate of deep defects[17,18].

A variety of efforts have been undertaken to address the Cu–Zn disorder issue in CZTSSe. Specifically, researchers have developed a range of cation substitution methods to increase the thermodynamic formation energy of Cu–Zn disorder[19–23]. However, whether the occupation of an external cation can relieve the disorder of intrinsic atoms in the material remains a subject of debate[6,24]. Researchers also started from the order–disorder phase-transition thermodynamics of the binary system, exploring a long-duration, low-temperature post-annealing strategy[16,25]. While an increased degree of ordering atomic and band-edge electronic structure were observed, this approach has not

[1]Beijing National Laboratory for Condensed Matter Physics, Renewable Energy Laboratory, Institute of Physics, Chinese Academy of Sciences (CAS), Beijing, People's Republic of China. [2]School of Physical Sciences, University of Chinese Academy of Sciences, Beijing, People's Republic of China. [3]School of Materials Science and Engineering, Peking University, Beijing, People's Republic of China. [4]Songshan Lake Materials Laboratory, Dongguan, People's Republic of China. [5]Center of Materials Science and Optoelectronics Engineering, University of Chinese Academy of Sciences, Beijing, People's Republic of China. [6]These authors contributed equally: Jinlin Wang, Fanqi Meng, Licheng Lou, Kang Yin. ✉e-mail: shijj@iphy.ac.cn; dmli@iphy.ac.cn; qbmeng@iphy.ac.cn

https://doi.org/10.1038/s41560-025-01902-w

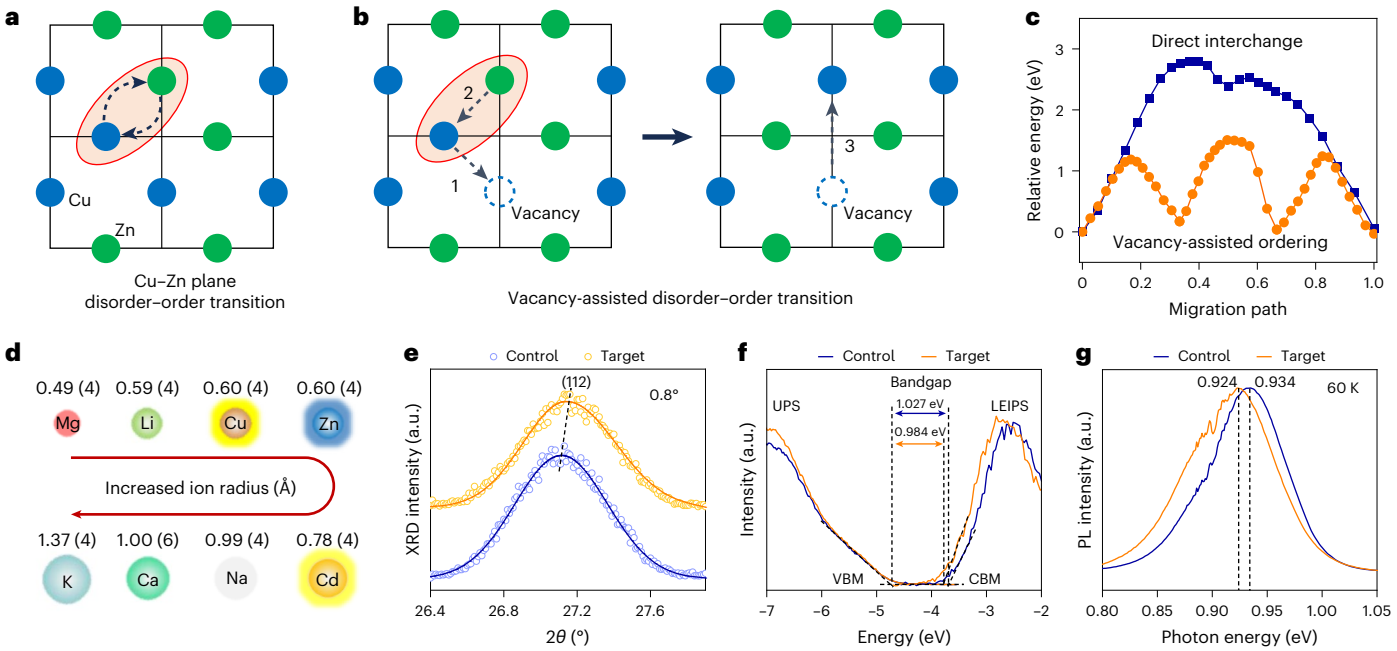

Fig. 1 | Atomic Cu–Zn interchange process and ion pre-doping. a,**b**, Schematic diagram of Cu–Zn interchange processes via direct (**a**) or V_{Cu}-assisted (**b**) mechanisms. **c**, Corresponding energy profiles along the interchange paths. **d**, Ionic radii[11] of several elements that can be used to form cation doping in the kesterite lattice. The number in parentheses indicates the coordination number. **e**–**g**, Grazing-incidence X-ray diffraction (XRD) of (112) peak of CZTSSe measured at an incidence angle of 0.8° (**e**), UPS valence and LEIPS conduction band-edge electronic structure (**f**), and steady-state PL spectra recorded at 60 K (**g**) of the pristine and target (Mg-doped) CZTSSe films. The black dashed line in **e** is a guide to the eye. The black dashed lines in **f** indicate the positions of the valence-band maximum (VBM) and conduction-band minimum (CBM) determined by the intersection between the background and the signal onset. The vertical dashed black lines in **g** indicate the PL peak positions.

yet translated into considerable device performance gains[6,26], probably because the long annealing also induced other negative effects such as surface atom volatilization loss and surface reconstruction. This has led to a stagnation in the regulation of Cu–Zn disorder, and even raised doubts about whether Cu–Zn disorder critically affects material quality and device performance[18,27]. Nevertheless, despite experimental challenges, recent theoretical studies have once again demonstrated a strong correlation between Cu–Zn disorder and the charge loss in CZTSSe[28], thereby reaffirming the necessity and urgency of addressing the Cu–Zn disorder issue.

Herein, we focus on the surface of CZTSSe film since it is believed to have a more significant impact on the solar cell performance[17,28]. Starting from the perspective of atomic ordering kinetics, we have developed a vacancy-assisted method to reduce the atom migration barrier and facilitate the Cu–Zn atomic ordering process. We intentionally introduced vacancy defects on the CZTSSe film surface through magnesium ion pre-doping followed by solution etching. This approach enhanced surface Cu–Zn ordering, effectively mitigating interface defects and carrier non-radiative recombination, while also promoting charge transport. Ultimately, we achieved an efficiency of 14.9% certified by the Chinese National PV Industry Measurement and Testing Center in a 0.27-cm^2 kesterite solar cell, as well as a certified efficiency of 13.3% in a 1.1-cm^2-area cell. This result represents significant advancement for emerging inorganic thin-film solar cells and open new opportunities for precise disorder–order control in crystalline materials.

Introduction of surface vacancies via Mg ion pre-doping

It was predicted that, under thermodynamic equilibrium, lower temperature would favour a higher degree of ordering in the Cu–Zn binary system[25,29]. However, from the perspective of kinetics, the system does not have sufficient energy at low temperature to drive the direct interchange of Cu–Zn atoms (schematically shown in Fig. 1a). This contradiction between thermodynamic favorability and kinetic limitations is probably a key factor restricting improvements in Cu–Zn ordering and, consequently, solar-cell performance.

Generally, the atom ordering kinetic rate is proportional to $\exp(-E_B/K_BT)$ (E_B is the energy barrier of atom interchange, K_B is the Boltzmann constant and T is the temperature)[30–32]. This suggests that reducing E_B can promote the atomic ordering process kinetically without sacrificing the final atomic ordering degree of the system. The introduction of vacancy defects is a promising way to reduce E_B because vacancies provide larger space to accommodate the interchanged atoms, as shown in Fig. 1a,b. Instead, direct interchange of atoms is primarily realized through the interstitial path, which is usually accompanied by large lattice deformation. We conducted first-principles calculations to estimate E_B for the Cu–Zn ordering processes via direct or vacancy-assisted interchange mechanisms. For the direct interchange E_B reached 2.8 eV (Fig. 1c), while for the vacancy mechanism (Cu vacancy, V_{Cu}) E_B was significantly reduced, to 1.3 eV, indicating that the kinetic rate of the ordering process can be enhanced by more than 16 orders of magnitude.

To experimentally realize the vacancy-assisted atom ordering we aim to introduce sufficient Cu vacancies in the region of interest in the CZTSSe film. We employed a strategy of ion pre-doping followed by solution etching to introduce vacancies in the film surface region. Group IA and IIA elements are potential candidates for doping in CZTSSe (Fig. 1d). In our experimental approach, the chlorides of these elements were first deposited onto the surface of CZTSSe precursor films. After selenization, the films were then etched using ammonia solutions to dissolve the doped ions and create surface vacancies. The films were subsequently annealed for about 1 h in a vacuum chamber (Ar, 0.2 Pa) to drive the Cu–Zn ordering process. Solar cells based on these films were finally fabricated after CdS, ZnO, ITO (Sn-doped In_2O_3) and Ni/Al depositions.

On the basis of the final solar cell performance (Supplementary Figs. 1–6), Li, Na and Cd were found to improve the average photoelectric conversion efficiency (PCE) by only ~0.1%, while K and Ca had a detrimental effect. The Mg element emerged as the most effective dopant, improving the average PCE from ~13.2% to ~14.8% without influencing the selenization process or the morphology of the CZTSSe absorber (Supplementary Figs. 7–9 and Supplementary Table 1). Thermal evaporation deposition of MgF_2 on the surface of the precursor film and spin-coating of a $MgCl_2$ solution yielded similar outcomes (Supplementary Fig. 10).

These results can be explained with the larger ion size of Na, K and Ca, which prevent effective doping at Cu or Zn sites[33–35]. Li and Cd can be incorporated into the lattice but are difficult to dissolve from the film during etching (Supplementary Fig. 11). In addition, Cd mainly dopes at the Zn site[36,37], where ordering via Zn vacancies has much higher E_B (~1.9 eV) compared with Cu vacancies (Supplementary Fig. 12).

Previous research demonstrated that Mg could dope at both Cu (Mg_{Cu}) and Zn (Mg_{Zn}) sites, with Mg_{Cu} even exhibiting negative formation energy in some cases[35,38–40]. From the perspective of Coulombic attraction and charge compensation, Mg_{Cu} also tend to form near the Cu_{Zn} site within the Cu–Zn disorder pair. These properties of the Mg ion and its induced V_{Cu} are conducive to the vacancy-assisted ordering process depicted in Fig. 1b.

We further characterized the Mg doping and its induced V_{Cu} in the film surface. For clarity, in the following, the undoped or the Mg-doped sample will be denoted as the control or target sample, respectively; the samples after being solution etched will be denoted as control (or target)-E; the etched and annealed samples will be denoted as control (or target)-E-A. Grazing-incidence X-ray diffraction found that the Mg incorporation made the (112) peak of CZTSSe slightly shift to a higher angle (Fig. 1e). Surface band-edge electronic-structure measurement using ultraviolet photoelectron spectroscopy (UPS) and low-energy inverse photoelectron spectroscopy (LEIPS) demonstrated that the Mg incorporation slightly reduced the bandgap of CZTSSe (Fig. 1f). Correspondingly, the steady-state photoluminescence (PL) of the doped film also showed a small redshift (Fig. 1g).

We also characterized these samples using scanning transmission electron microscopy and electron energy loss spectroscopy (EELS). As in Supplementary Fig. 13, the existence of the Mg element in the top region of the CZTSSe crystal can be seen in the target sample. By further analysing three selected regions from the surface to the bulk, a negative correlation between Mg and Cu EELS intensity was also observed. Energy dispersive X-ray spectroscopy (EDX) was also used to demonstrate the existence of the Mg element in kesterite crystals. As shown in Supplementary Figs. 14 and 15, the Mg Ka EDX signal can be observed in the target sample. This result was further confirmed by using pure sulfide Cu_2ZnSnS_4 as the studied sample, in which the Mg Ka EDX signal can be clearly distinguished without any interference. All these results support the view that Mg has doped into the CZTSSe lattice, especially at the Cu site.

Using EDX characterization, the solution etching of Mg from the kesterite crystals was also demonstrated in the target-E sample, reflected by the disappearance of Mg EDX signal from the Cu_2ZnSnS_4 sample and reduced spectral intensity in the Mg EDX signal region in the CZTSSe sample. EELS of target-E samples also exhibited significant reductions or disappearance of the Mg signals (Supplementary Fig. 16). Inductively coupled plasma optical emission spectroscopy-based quantitative characterization further confirmed a pronounced reduction in the overall Mg content in the films after etching (Supplementary Table 2). These results were also supported by X-ray photoelectron spectroscopy and secondary-ion mass spectroscopy results (Fig. 2d and Supplementary Figs. 17 and 18), collectively demonstrating that the Mg element doped in CZTSSe has been sufficiently dissolved away.

We further measured atomic-resolution HAADF–scanning transmission electron microscopy images to investigate the influence of solution etching on the V_{Cu} properties of the control-E and target-E samples (Fig. 2a–c and Supplementary Fig. 19). In these two samples, the atomic images of CZTSSe lattice observed along the [0 -1 0] or [0 1 0] direction were captured from the top region of the films, in which the (002) planes comprising Sn and Cu cations and Sn cations with higher HAADF intensity can be clearly distinguished, as shown in Fig. 2a. For clarity, the corresponding atom structure of CZTSSe is schematically given. By profiling the Cu–Sn chain of the target-E sample, lower HAADF intensity can be observed at some Cu sites (Fig. 2b), which can be attributed to the existence of V_{Cu}. For comparing to the control-E sample, we have conducted a statistical analysis of the HAADF intensity of Cu and Sn sites along Cu–Sn cations in these two samples. Cu/Sn intensity ratio was used to reflect the average concentration of V_{Cu} in CZTSSe. As shown in Fig. 2c, the target-E sample exhibited an obviously lower Cu/Sn intensity ratio, indicating higher V_{Cu} concentration.

We also performed Raman spectra measurement to confirm the V_{Cu} results in these two sample groups. The Raman spectra were fitted on the basis of the lattice vibration modes of CZTSSe[41,42], with the detailed fitting results presented in Fig. 2e,f, Supplementary Fig. 20 and Supplementary Table 3. The intensity ratio between different Raman peaks ($R = A_{172}/(A_{172} + A_{194})$ is used to reflect V_{Cu} in CZTSSe, in which lower value of R stands for higher V_{Cu} concentration[41]. As shown in Fig. 2e, the R value of the control sample was only a little reduced after the solution etching, indicating that the V_{Cu} concentration was slightly increased. Comparatively, a significant decrease in the R value was observed in the target sample (Fig. 2f), suggesting an obvious increase in the V_{Cu} concentration. In addition, the R value of the target-E sample was also obviously smaller than that of the control-E sample. These results supported that the Mg pre-doping and solution etching had effectively introduced V_{Cu} in the film surface. In addition, we observed that Mg doping and surface etching also caused Raman peak shifts in these samples. However, interpreting the underlying physical mechanisms responsible for these shifts remains a challenge which requires more fundamental research on the vibrational properties of kesterite lattice containing complex structural defects.

Vacancy-enhanced Cu–Zn atomic ordering

We further investigated the annealing induced Cu–Zn ordering in the CZTSSe lattice. Using Kelvin-probe force microscopy, the surface contacting potential difference (CPD) of these films were first measured (Fig. 3a,b and Supplementary Fig. 21). As shown in Fig. 3a, the solution etching process caused the CPD of the control and target films to decrease by ~90 mV and ~190 mV, respectively. The larger CPD reduction in the target sample suggests the more effective formation of V_{Cu} acceptors (Supplementary Note 1). After the annealing, the CPD of both films moved to higher values (Fig. 3b), and the target film exhibited a much larger increase (283 mV) compared to the control film (160 mV). This indicates that the density of acceptors was more significantly reduced in the target-E-A film. Cu–Zn ordering process could be an important cause to reduce Cu_{Zn} acceptors[18].

We used Raman spectroscopy to gain further evidence for the enhancement in the Cu–Zn ordering in the target-E-A film[43,44]. As shown in Fig. 3c and Supplementary Fig. 22, compared to the as-selenized target film, the solution etching and annealing processed sample present a shift of the Raman peak of kesterite phase to a higher wavenumber position, also accompanied by a narrowing of the Raman peak. In particular, a double peak structure appeared in the wavenumber region between 160 and 180 cm^{-1} in the final target-E-A sample. Comparatively, no such phenomena were observed in the control sample; especially the control-E-A sample still exhibited a single-peak structure in the (160, 180 cm^{-1}) wavenumber region. These characteristics in Raman spectra well support the enhancement of Cu–Zn ordering in the target CZTSSe[43,44]. Optical bandgap of CZTSSe is another signature related to the Cu–Zn ordering degree[15,16], which we evaluated by reflectance spectroscopy (Fig. 3d and Supplementary Fig. 23). The result shows

https://doi.org/10.1038/s41560-025-01902-w

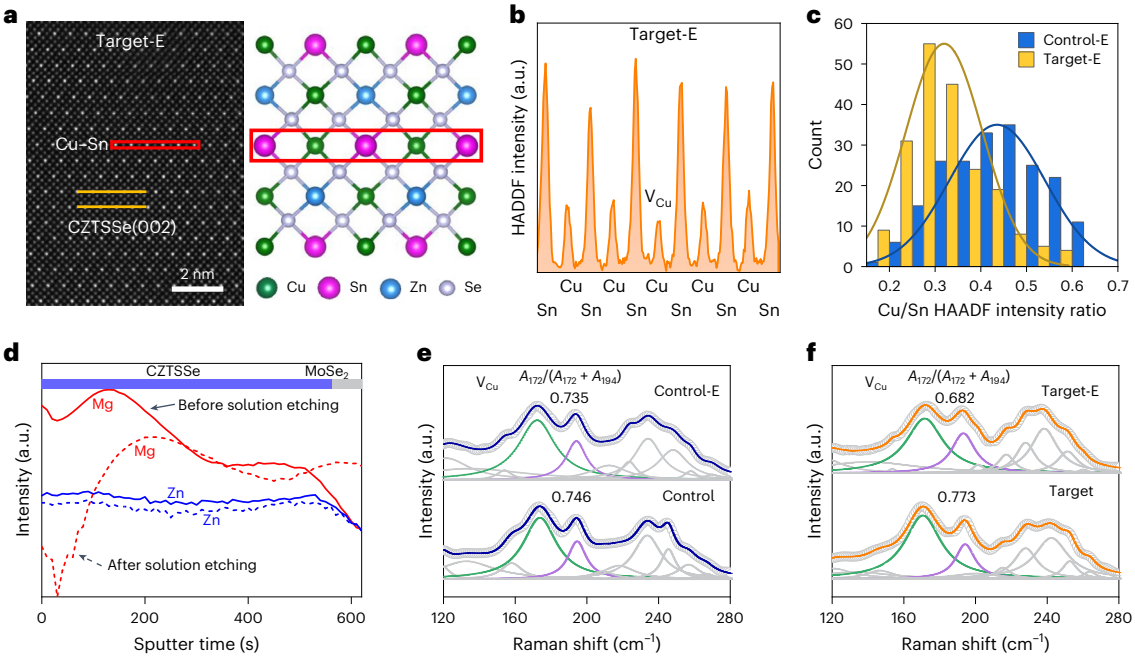

Fig. 2 | Atomic vacancy formation. a, Filtered atomic-resolution HADDF image captured from the surface region of the target-E film. Corresponding atom arrangement is given for clarity. **b**, Intensity profile of the Cu–Sn cation chain in the (002) plane as marked by red rectangle. The Cu vacancy is labelled according to the intensity. **c**, Histograms of the Cu/Sn HAADF intensity ratio of control-E and target-E sample. Each Cu/Sn ratio value in this statistic was calculated from one Cu atom and its nearest neighbouring Sn atom in the Cu–Sn chain. Two hundred pairs of randomly selected Cu and corresponding Sn sites have been included here. **d**, TOF–secondary-ion mass spectroscopy elemental depth profiles of Zn and Mg of the Mg-doped CZTSSe films before and after solution etching. The CZTSSe/$MoSe_2$ film structure is schematically depicted by a horizontal bar. **e**,**f**, Raman spectra (excited at 325 nm) of control (**e**) and Mg-doped (**f**) CZTSSe films before and after solution etching. Blue and orange solid lines on top of raw data are the sum fitting curves of the control and Mg-doped film (Lorentzian fitting), respectively. Green, purple and grey lines represent the individual fitting curves corresponding to the lattice vibration modes of CZTSSe[41,42] (Supplementary Table 3).

that, after the etching and annealing process, the bandgap of the target sample increased more than that of the control sample, up to ~95 meV (Fig. 3d). This increase in the bandgap was further demonstrated by UPS and LEIPS. As seen in Fig. 3e, the bandgap of target film surface increased by ~130 meV, realized by the shift of both the valence and the conduction band edge. This was also reflected in the steady-state PL spectra. The PL peak of the target-E-A sample shifted to 0.951 eV (Fig. 3f), a larger shift than that of the control-E-A and pristine target samples (Fig. 1f). Overall, these characterization results demonstrated that our proposed strategy (Mg pre-doping, solution etching and annealing) had effectively improved the Cu–Zn ordering of CZTSSe films.

Defect and charge-loss characterization

We further investigated the influence of improved Cu–Zn ordering on the defect and charge-loss properties of the fabricated kesterite solar cells. The energetic distribution and charge-capturing properties of defects in the cells were characterized using thermal admittance spectroscopy (TAS) method (Fig. 4a,b and Supplementary Fig. 24). As the Arrhenius plots shown in Fig. 4a, the ionization energy (E_t) of defects in the two samples did not exhibit essential difference, both in the range between 100 and 200 meV corresponding to Cu_{Zn} defect[14,45,46]. Differently, the defect attempt-to-escape frequency (ν_0) of the target sample ($2.1 \times 10^9\ s^{-1}$, corresponding charge-capturing cross-section (σ) of $7.28 \times 10^{-17}\ cm^{-2}$) was found to be ~15 times smaller than that of the control sample ($3.4 \times 10^{10}\ s^{-1}$, corresponding σ of $1.17 \times 10^{-15}\ cm^{-2}$), indicating that the defect charge-capturing velocity was largely reduced. The result suggests an increased atomic ordering, which reduces the electron–lattice vibration interaction in the solid material[34].

We further quantified the defect density using different capacitance analysis methods. First, TAS results exhibited that the density of Cu_{Zn} defect in the target sample was $9.8 \times 10^{15}\ cm^{-3}$ (Supplementary Note 2), which was only half of that in the control sample, demonstrating the reduced Cu–Zn disordering (Fig. 4b). We measured more specific spatial distribution of the defect charge by capacitance–voltage (C–V) and drive-level capacitance profiling (DLCP) methods. As shown in Fig. 4c, the target sample exhibited much lower charge concentration in the measured region due to the reduced Cu_{Zn} acceptors. Particularly, the interface defect density of the target sample (N_{it}, estimated from the difference in the charge density measured by C–V and DLCP) was only one fourth of that in the control sample.

We also used an extended physics model to investigate the charge-capturing properties of interface defects[47] (Supplementary Fig. 25). Through fitting the frequency-dependent admittance curve, the density of interface defects that participated in the charge capturing in the target sample was estimated to be $3.26 \times 10^{14}\ cm^{-2}\ eV^{-1}$, which was only 1/10 of that in the control sample (Fig. 4d). The fitting result also indicated that the target sample had much higher resistance of interface charge capturing (R_{it}), that is, more difficult interface charge capturing. Temperature-dependent PL was also measured to investigate the influence of reduced Cu–Zn disordering on the activity of Sn_{Zn} deep defect[10]. The results (Supplementary Fig. 26) showed that the target sample had an obviously larger PL quenching activation energy (66 meV) than that of the control one (37 meV), indicating lower activity of charge non-radiative transitions. The PL quenching activation energy of the target sample is also very close to the predicted carrier-capture energy barrier of Sn_{Zn} defect in ordered kesterite lattice, which further supported improved Cu–Zn ordering[48].

The aforementioned defect characterization demonstrated that the density and charge capturing velocity of defects, especially

https://doi.org/10.1038/s41560-025-01902-w

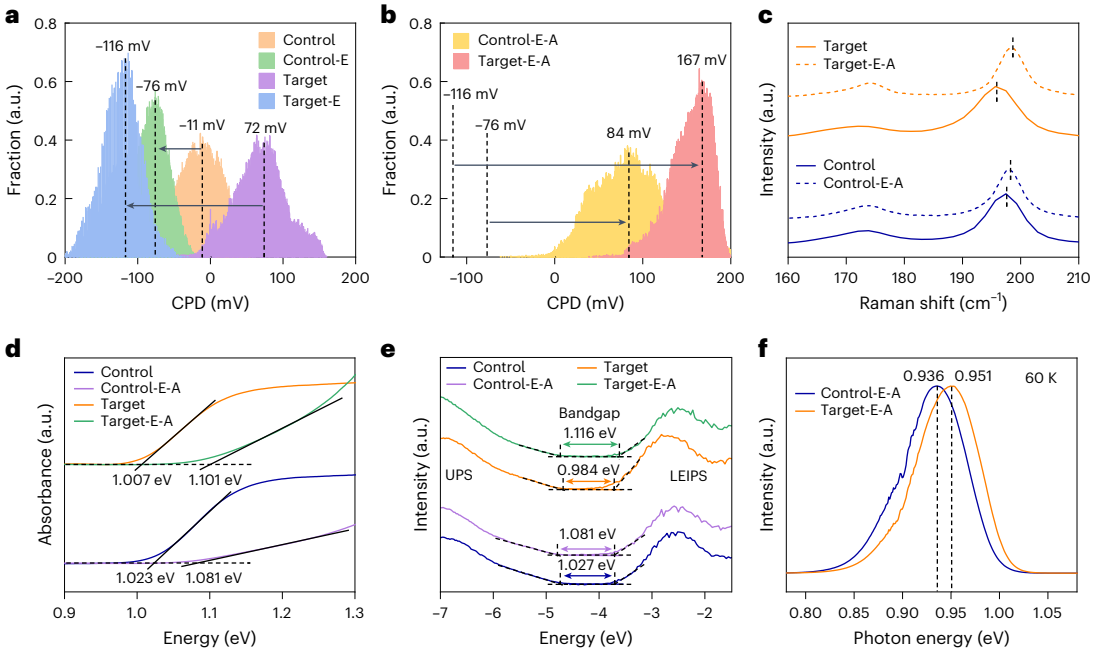

Fig. 3 | Vacancy enhanced atomic ordering. a, CPD of the control and target films before and after solution etching. **b**, CPD of the control and target films after being annealed. The black dashed lines in **a** and **b** show the CPD maximum, and the arrows indicate the movement of CPD. **c**, Raman spectra acquired under 532 nm laser excitation (detailed spectral fitting provided in Supplementary Fig. 22). **d**, UV–visible absorption spectra transformed from reflectance spectra. **e**, UPS and LEIPS spectra of the films before and after experiencing the atomic ordering process. The vertical dashed black lines in **c** indicate the Raman peak position. The solid lines in **d** represent the linear extrapolation of the UV–visible absorption onset used to estimate the bandgap. The estimated bandgaps are 1.023 and 1.081 eV for the control and control-E-A films, and 1.007 and 1.101 eV for the target and target-E-A films, respectively. In **e**, the position of the valence-band maximum and conduction-band minimum (depicted by vertical dashed lines) of these samples are determined by the intersection between the background and the signal onset (dashed black lines). Arrows show the bandgaps of these samples. The bandgaps are 1.027 and 1.081 eV for the control and control-E-A films, and 0.984 and 1.116 eV for the target and target-E-A films, respectively. **f**, Steady-state PL spectra of the control-E-A and target-E-A films. The vertical dashed black lines indicate the PL peak position.

the interface defect, have been significantly suppressed through the Cu–Zn ordering process. As a result, the target cell obtained more superior open-circuit voltage (V_{OC}) at temperatures ranging from 300 to 100 K and moreover higher recombination activation energy, E_A, than that of the control cell (Fig. 4e). The very small discrepancy between E_A and optical bandgap (Supplementary Fig. 27) indicated that the fast subgap relaxation of photogenerated carriers had become negligible in the target CZTSSe sample, further confirming that localized electronic states caused by the Cu–Zn disordering had been suppressed[6,12,13].

We also characterized the charge dynamics of the cells using modulated electrical transient methods[49,50]. As in Fig. 4f, the target cell exhibited much longer photovoltage decay lifetime and moreover obviously reduced fast decay in the early stage. This phenomenon implies that the interface charge recombination in the cell has been suppressed, agreeing well with the defect characterization results. For the transient photocurrent, the target cell exhibited obviously smaller decay time than the control cell (Fig. 4g,h). In addition, the photocurrent peak position of the target cell almost kept constant at different bias voltages, significantly distinct to the control cell whose photocurrent peak moved continuously with the voltage increase. These phenomena indicated that the target cell had better charge transport ability. The elimination of localized subgap electronic states and their induced charge trapping and detrapping processes is an important beneficial reason for this result. The improved charge transport ability should be able to help more photoinduced carriers in the CZTSSe absorber be extracted into the buffer/window layer, especially when the built-in electric field was reduced at high voltages. This was confirmed by the higher charge extraction efficiency (η_{ext}) quantified from the modulated electrical transient results[51] (Fig. 4i). In addition, due to the reduced interface charge recombination, the extracted charge in the window layer can also be collected by the electrodes more efficiently, resulting in higher charge collection efficiency (η_C). The reduction in bulk and interfacial charge loss is expected to improve PCE of the cell.

Device performance characterization

To obtain the optimal Cu–Zn ordering result, we have systematically optimized the Mg pre-doping concentration and the subsequent annealing temperature. The performance parameters of the cells obtained from different nominal annealing temperatures are shown in Fig. 5a. As can be seen, average PCE of the target cell was enhanced from ~13.7% to ~14.6% when the temperature increased from 180 to 220 °C. This enhancement was reflected in all three performance parameters, V_{OC}, short circuit current (J_{SC}) and fill factor (FF). Particularly, the average FF was improved from ~0.69 to ~0.72, and the average V_{OC} reached 550 mV in the optimal group, confirming the reduced charge recombination in the cell. Comparatively, the PCE of the control cell was only enhanced by ~0.1% (from 13.1% to 13.2%). This result agrees well with the fact that the atomic ordering was limited in the control cell.

The current density–voltage (J–V) characteristics of the champion cells are given in Fig. 5b. The target cell achieved a high total-area PCE of 15.4% with J_{SC} of 37.4 mA cm^{-2}, V_{OC} of 557.6 mV and FF of 0.737. All these performance parameters are much superior to that of the control cell which exhibited a PCE of 13.7%. One of the cells in the target group was sent to an accredited independent laboratory (National PV Industry Measurement and Testing Center, NPVM) for certification. The certified PCE (J–V measurement; Fig. 5c) reached 14.9% (Supplementary Fig. 28), representing a substantial advancement for

https://doi.org/10.1038/s41560-025-01902-w

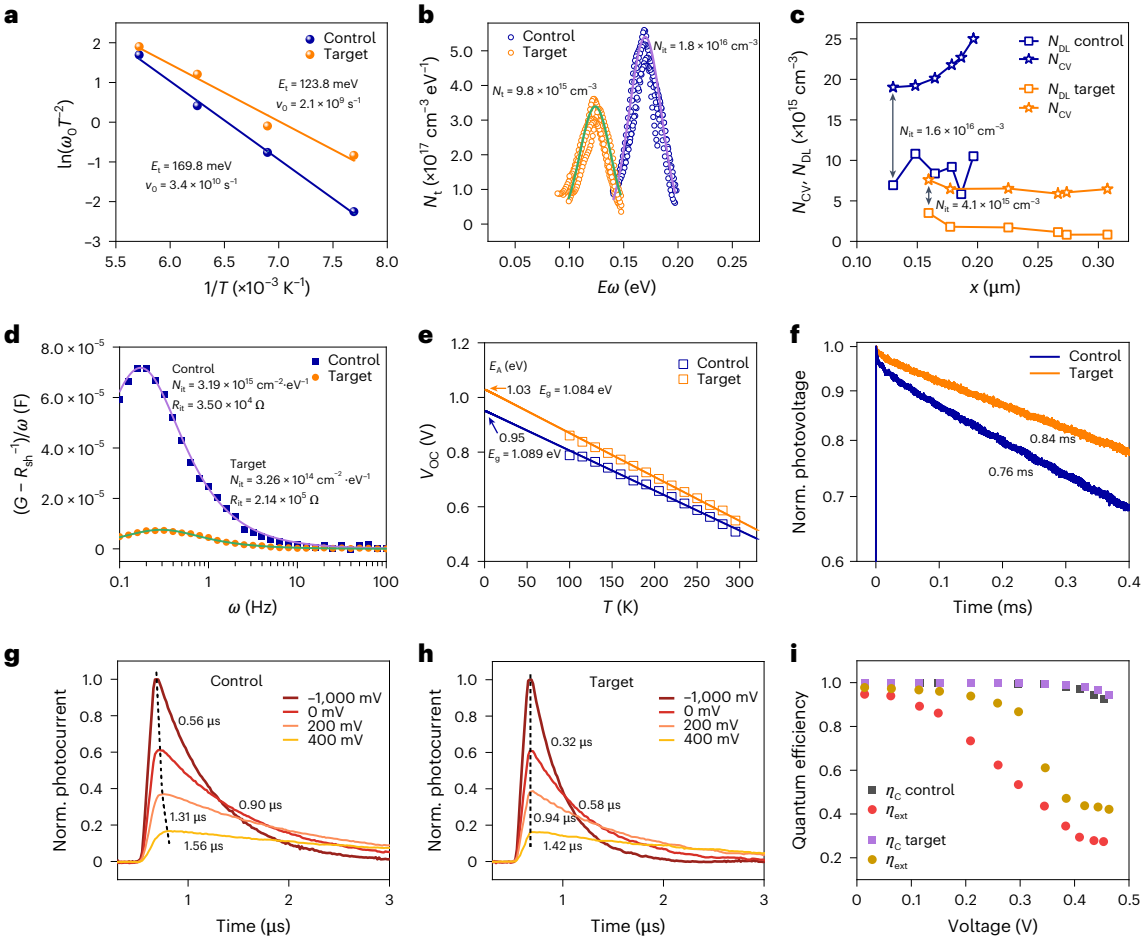

Fig. 4 | Defect and charge-loss characterization of kesterite solar cells. **a**, The Arrhenius plots of the inflection frequencies (ω_0) determined from the derivative of the admittance spectra. The solid lines are fittings of the Arrhenius plots using $\omega_0 = 2\pi\nu_0 T^2\exp(-E_t/(K_B T))$, where E_t is the defect ionization energy and ν_0 is the attempt-to-escape frequency (Supplementary Note 2). The fitted E_t values of the control and target samples are 169.8 and 123.8 meV, respectively, and the corresponding ν_0 are 3.4×10^{10} and 2.1×10^9 s^{-1}, respectively. **b**, The energetic distribution of defects derived from thermal admittance spectra. The solid lines are the Gaussian fit to the respective defect energy level. The fitted defect densities are 1.8×10^{16} cm^{-3} for control sample and 9.8×10^{15} cm^{-3} for target sample. **c**, Charge profiles in the CZTSSe absorber layer derived from capacitance–voltage (N_{CV}) and drive-level charge profiling (N_{DL}) measurements. The vertical arrows depict the difference between N_{DL} and N_{CV}, estimating the interface defect density (N_{it}). **d**, Quantification of the interface defect in the cell using frequency-dependent admittance (G) analysis. Solid lines on top of raw data are the fitted curves between $(G - 1/R_{sh})/\omega$ and angular frequency (ω) (detailed model and fitting formulae can be found in the literature[47]). R_{sh} is the shunt resistance of the cell. The interface defects densities (N_{it}) are 3.19×10^{15} and 3.26×10^{14} cm^{-2} eV^{-1} for the control and target samples, and the corresponding interface charge-capturing resistances (R_{it}) are 3.50×10^4 and 2.14×10^5 Ω, respectively. **e**, Temperature-dependent open-circuit voltage (V_{OC}) of the cells. E_g shows the bandgap of control and target cells. The arrows refer to the activation energy E_A which is obtained from the value of the intercept with the y axis ($T = 0$ K). **f**, Photovoltage decay dynamics of the cells at 0 V. **g**,**h**, Photocurrent decay dynamics of the control and target cells at different bias voltages. The dashed lines depicted the evolution of photocurrent peaks. The exponential decay times were 0.56, 0.90, 1.31 and 1.56 μs (**g**) and 0.32, 0.58, 0.94 and 1.42 μs (**h**) for −1000, 0, 200 and 400 mV, respectively. **i**, Charge extraction (η_{ext}) and collection (η_C) efficiencies of the cells derived from the modulated electrical transient measurements.

emerging inorganic thin-film solar cells. The cell also exhibited excellent operational stability in the process, also demonstrating a steady-state PCE of 14.9% under maximum power point tracking (MPPT) over 300 s (Fig. 5d).

We also fabricated 1.1 cm^2-area solar cells and achieved 13.3% certified PCE (J–V, certification report and MPPT; Fig. 5e and Supplementary Figs. 29–31), outperforming the existing published results in this field to the best of our knowledge. The realization of this performance primarily benefited from high uniformity of photoelectric properties of the cell at the centimetre scale. As the electroluminescence (EL) characterization[52,53] shown in Fig. 5f, the target cell exhibited uniform EL in the whole active region, while only part region of the control cell can be lit up under charge injection. Therefore, our vacancy strategy not only enables more efficient atomic ordering, but also enables this process to occur more synchronously at different spatial locations. These benefits make this strategy suitable to preparing larger-sized CZTSSe solar modules.

Conclusions

To address the thermodynamic and kinetic limitations associated with cation ordering in CZTSSe crystal materials, we have designed a vacancy-assisted strategy to reduce the cation exchange barrier for enhancing atomic exchange dynamics. By introducing atomic vacancies through magnesium pre-doping and solution etching followed by low-temperature thermal treatment, we improved the Cu–Zn ordering within the surface region of CZTSSe films. This approach suppressed surface defects and charge losses in CZTSSe and thus enabled us to achieve an efficiency of 14.9%. This represents a step forward in the performance of CZTSSe solar cells and open new opportunities for the development of inorganic thin-film

https://doi.org/10.1038/s41560-025-01902-w

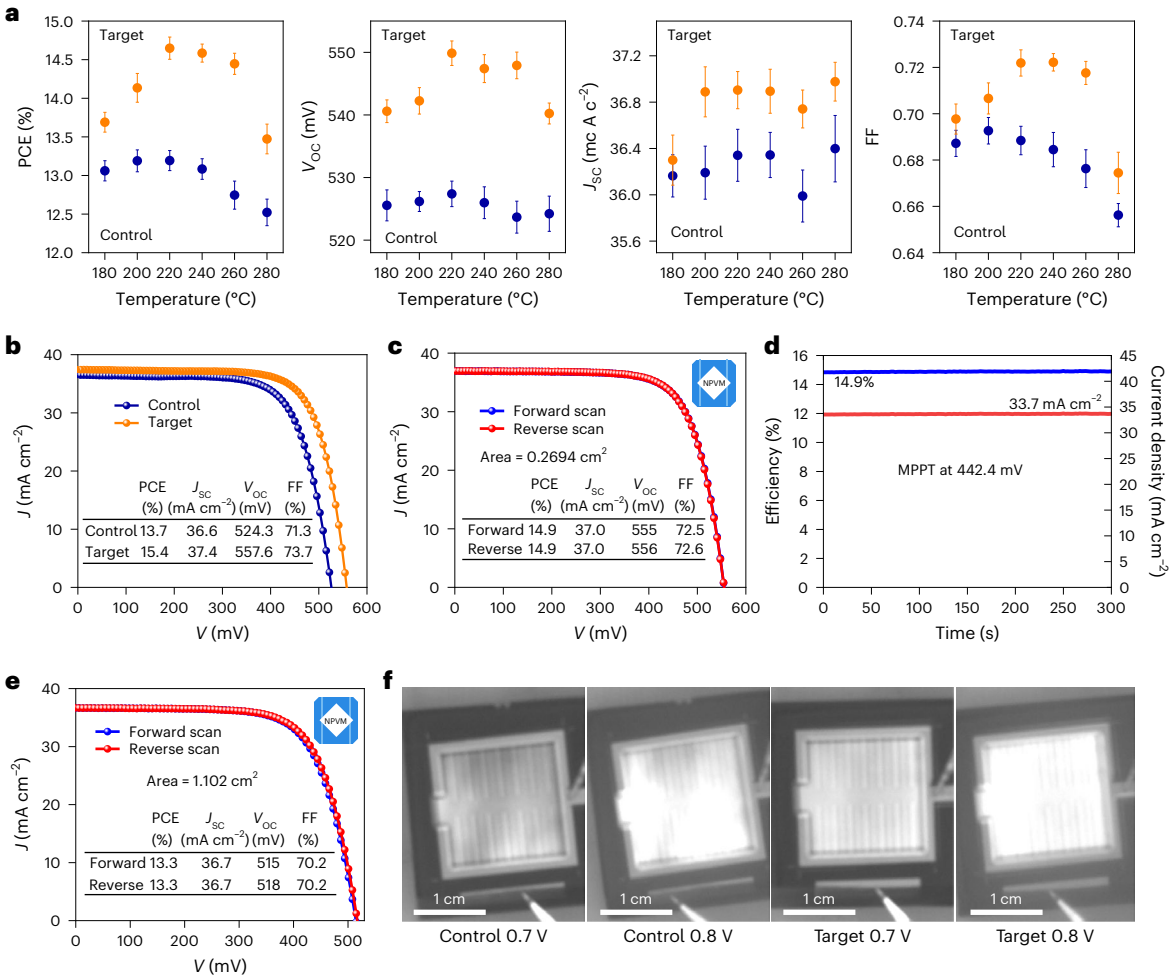

Fig. 5 | Solar cell performance. a, Statistical performance parameters of the cells with CZTSSe films annealed at different nominal temperatures. Mean and error bar are displayed in the interval chart. Error bars, 95% confidence interval. Eighteen cells are included in the statistics. **b**, Current density–voltage (*J*–*V*) characteristics of champion devices. **c**,**d**, Certified *J*–*V* (c) and maximum power point tracking curves (300 s; **d**) of the champion target device (0.27 cm^2). **e**, Certified *J*–*V* curves of the large-area device (1.1 cm^2). **f**, Electroluminescence images of the control and target devices.

photovoltaics. Moreover, the atomic ordering strategy might be extended to other multi-elemental crystalline materials to regulate their atomic structure.

Methods

Materials

CuCl (99.999%, Alfa), $ZnAc_2$ (99.99%, Aladdin), $SnCl_4$ (99.998%, Macklin), AgCl (99.5%, Innochem), $CdCl_2$ (99.99%, Aladdin), 2-methoxyethanol (99.8%, Aladdin), thiourea (99.99%, Aladdin, recrystallized before using), $MgCl_2$ (99.9%, Aladdin), MgF_2 (99.9%, Alfa), LiCl (99.9%, Alfa), NaCl (99.998%, Alfa), KCl (99.997%, Alfa), $CaCl_2$ (99.99%, Innochem), methanol (99.9%, Innochem), Se pellets (99.999%, Zhong Nuo Advanced Material), $CdSO_4 \cdot 8/3H_2O$ (99.99%, Aladdin), ammonium chloride (≥99.5%, Sinopharm Chemical Reagent) and ammonia (25.0 ~ 28.0%; Sinopharm Chemical Reagent) were used in this work. These chemicals except thiourea were used directly without further purification.

Precursor-solution and film preparation

The precursor solution was prepared as follows: first, thiourea was dissolved in 2-methoxyethanol (MOE), followed by the addition of CuCl, which was then dissolved with stirring at 50 °C to yield a colourless solution. Subsequently, AgCl was introduced into this solution and stirred for 1 hour to obtain Solution 1. Secondly, the MOE was added to a bottle containing $SnCl_4$ to produce a colourless solution. $Zn(Ac)_2$ and $CdCl_2$ was then dissolved in the Sn-containing solution to form solution 2. Thirdly, solutions 1 and 2 were mixed to give the final precursor solution. In the precursor solution, the concentrations of metal elements and thiourea are 1.88 M and 3.20 M, respectively. The molar ratio of (Ag+Cu)/(Zn+Cd+Sn), (Zn+Cd)/Sn, Ag/(Ag+Cu), Cd/(Cd+Zn) and thiourea/metal are 0.75, 1.12, 0.10, 0.06 and 1.7, respectively.

The kesterite precursor films were prepared by spin-coating the precursor solution on cleaned Mo substrates, followed by annealing on a 280 °C hot plate in the air. The coating and annealing procedures were iteratively performed to achieve a target thickness of approximately 2 μm for the precursor films.

Surface treatment with metal chlorides or MgF_2

$MgCl_2$, LiCl, NaCl, KCl, $CaCl_2$ and $CdCl_2$ were dissolved in methanol to prepare the solution with the concentration of 2.5 to 10 mg·ml^{-1}. Here, all the chloride solutions were prepared in a N_2-filled glovebox. The solutions were magnetically stirred at room temperature until fully dissolved. The chloride solution at different concentrations was coated onto the surface of the precursor film, followed by annealing on a 200 °C hot plate for 1 min. Mg-containing precursor was also prepared by thermal evaporation of MgF_2 with different thicknesses (3, 7, 11 and 15 nm). These films were then selenized at about 535 °C for about 20 min in a graphite box under N_2 atmosphere using RTP furnace.

Film surface etching and annealing

The selenized film was immersed into an ammonia aqueous solution bath at 70 °C (10 ml ammonia in 200 ml deionized water) for about 12 min, aiming to remove the doped Mg in the film surface region to artificially introduced cation vacancies. After washing and air drying, the film was annealed at about 180 ~ 280 °C for about 60 min in a vacuum chamber (Ar, 0.2 Pa).

Device fabrication

CdS buffer (~50 nm), ZnO (~40 nm, sputtering power: 55 W, gas source: Ar, pressure: ~2 Pa) and ITO (~200 nm, sputtering power: 60 W, gas source: Ar, pressure: ~0.2 Pa) window layer were subsequently deposited onto the CZTSSe film via CBD and magnetron sputtering, respectively. The Ni (~50 nm)/Al (~2 µm) grid electrode and MgF_2 antireflective coating (~100 nm) were then deposited through thermal evaporation. The cells were separated from each other by mechanical scribing and the designed area of an individual cell is 0.28 cm^2 (4 × 7 mm^2; Supplementary Fig. 27).

Film characterization

The crystallographic structure of the films was analysed using X-ray diffraction obtained from a PANalytical X-ray diffractometer, employing Cu Kα radiation as the source. Raman spectroscopy was conducted using a LabRAM HR Evolution (HORIBA) spectrometer, with 532 nm and 325 nm lasers as the excitation sources. LEIPS and UPS were performed on a multifunctional photoelectron spectrometer (AXIS ULTRA DLD). Elemental depth compositional profiles of films were determined by secondary-ion mass spectroscopy (ToF-SIMS 5, Germany ION-ToF GmbH). The quantitative characterization of elements is carried out using inductively coupled plasma optical emission spectroscopy (Agilent ICP-OES 725 ES). The morphology of film was examined using SEM with a Hitachi S4800 instrument. The microstructure and elemental distribution were also measured using a JEOL-F200CF scanning transmission electron microscope with an EDX system. EELS was obtained using a beam of an electron microscope. X-ray photoelectron spectroscopy was executed on an ESCALAB 250Xi (Thermo Fisher Scientific) system, where argon ion etching was applied to facilitate depth profiling. Both steady-state and transient PL spectra were acquired using an FLS 900 PL spectrometer from Edinburgh Instruments, which was excited by a picosecond-pulsed laser operating at approximately 640 nm and coupled with a liquid helium cooling system. KPFM images were captured using a Multimode 9 atomic force microscope from Bruker. The UV–visible diffuse reflectance spectra were recorded on a Shimadzu UV-3600 spectrophotometer.

Device characterization

The *J*–*V* characteristics of the photovoltaic cells were measured using a Keithley 2601 Source Meter under simulated AM 1.5 G solar illumination at an intensity of 100 mW cm^{-2}. Calibration was performed using a silicon reference cell, which was calibrated by the National Institute of Metrology of China. The voltage sweep ranged from −50 mV to 600 mV at a scan rate of approximately 90 mV s^{-1}. Cell certification was performed at the NPVM, confirming a certified aperture area of 0.2694 cm^2 for the cell. All measurements were conducted under ambient conditions (air, 25 °C, uncontrolled humidity), with no preconditioning steps before the measurements. The external quantum efficiency (EQE) was determined using an Enlitech QE-R system, which employed calibrated silicon (Si) and germanium (Ge) diodes for reference. Frequency-dependent admittance/capacitance spectra were acquired using a Princeton Versa STAT3 electrochemical workstation in the absence of illumination, with the scanning frequency ranging from 0.1 Hz to 10^6 Hz. The temperature of the cell was meticulously regulated by a Lakeshore TTPX low-temperature probe station. *C*–*V* profiles, DLCP and temperature-dependent *J*–*V* characteristics were all measured utilizing the Princeton Versa STAT3 electrochemical workstation. Modulated transient photocurrent and photovoltage (M-TPC/TPV) measurements were obtained by a tunable nanosecond laser pumped at 640 nm and recorded by a subnanosecond resolved digital oscilloscope (Tektronix, DPO 7104) with a sampling resistance of 50 Ω or 1 MΩ (refs. 49–51). EL characterization was performed using a vis–NIR CMOS camera (Spark-Opt, CIS-CM990) covering a spectral range of 400-1700 nm.

DFT calculation

All calculations were carried out under the scheme of spin-polarized density functional theory (DFT) using CASTEP[54]. Specifically, the exchange–correlation energy was described by the Perdew–Burke–Ernzerhof (PBE) function[55] within the framework of the generalized gradient approximation (GGA). The criteria for geometric convergence were stringently defined, with a maximum force threshold of 0.03 eV/Å, an energy change ceiling of 10^{-5} eV/atom, a maximum displacement of 0.001 Å and a maximum stress of 0.5 GPa. The sampling in the Brillouin zone was set with 3 × 3 × 1 by the Monkhorst–Pack method.

The diffusion of Cu/Zn was investigated by searching the possible diffusion route and identifying the migration transition state with the lowest diffusion energy barrier. The diffusion energy barrier is the energy difference between the total energies of transition state and the initial structure. The transition state is searched by the generalized synchronous transit (LST/QST) method[56] implemented in the CASTEP code. The algorithm starts from a linear synchronous transit (LST) optimization and continues with a quadratic synchronous transit (QST) maximization process. Thereafter, the conjugate gradient (CG) minimization is conducted from the obtained LST/QST structure to refine the geometry of transition state. The LST/QST/CG calculations are repeated till a stable transition state is obtained.

Reporting summary

Further information on research design is available in the Nature Portfolio Reporting Summary linked to this article.

Data availability

The main data supporting the findings of this study are available within the main text, Supplementary Information and source data files. Source data are provided with this paper.

References

1. Ranna, A. et al. Disorder-induced suppression of superconductivity in infinite-layer nickelates. *Phys. Rev. Lett.* **135**, 126501 (2025).
2. Roychowdhury, S. et al. Enhanced atomic ordering leads to high thermoelectric performance in $AgSbTe_2$. *Science* **371**, 722–727 (2021).
3. Saglam, H. et al. Entropy-driven order in an array of nanomagnets. *Nat. Phys.* **18**, 706–712 (2022).
4. Chen, R. et al. Entropy-driven multiscale defects enhance the thermoelectric properties of ZrCoSb-based half-Heusler alloys. *Chem. Eng. J.* **455**, 140676 (2023).
5. Chen, S., Walsh, A., Gong, X. G. & Wei, S. H. Classification of lattice defects in the kesterite Cu_2ZnSnS_4 and $Cu_2ZnSnSe_4$ earth-abundant solar cell absorbers. *Adv. Mater.* **25**, 1522–1539 (2013).
6. Shin, D., Saparov, B. & Mitzi, D. B. Defect engineering in multinary earth-abundant chalcogenide photovoltaic materials. *Adv. Energy Mater.* **7**, 1602366 (2017).
7. Park, J. S., Kim, S., Xie, Z. & Walsh, A. Point defect engineering in thin-film solar cells. *Nat. Rev. Mater.* **3**, 194–210 (2018).
8. Wang, W. et al. Device characteristics of CZTSSe thin-film solar cells with 12.6% efficiency. *Adv. Energy Mater.* **4**, 1301465 (2014).

9. Gong, Y. et al. Elemental de-mixing-induced epitaxial kesterite/CdS interface enabling 13%-efficiency kesterite solar cells. *Nat. Energy* **7**, 966–977 (2022).
10. Shi, J. et al. Multinary alloying for facilitated cation exchange and suppressed defect formation in kesterite solar cells with above 14% certified efficiency. *Nat. Energy* **9**, 1095–1104 (2024).
11. Weller, M., Weller, M. T., Overton, T., Rourke, J. & Armstrong, F. *Inorganic Chemistry* (Oxford Univ. Press, 2014).
12. Gokmen, T., Gunawan, O., Todorov, T. K. & Mitzi, D. B. Band tailing and efficiency limitation in kesterite solar cells. *Appl. Phys. Lett.* **103**, 103506 (2013).
13. Scragg, J. J. S. et al. Cu–Zn disorder and band gap fluctuations in $Cu_2ZnSn(S,Se)_4$: theoretical and experimental investigations. *Phys. Status Solidi b* **253**, 247–254 (2015).
14. Chen, S., Gong, X. G., Walsh, A. & Wei, S.-H. Defect physics of the kesterite thin-film solar cell absorber Cu_2ZnSnS_4. *Appl. Phys. Lett.* **96**, 021902 (2010).
15. Grossberg, M., Krustok, J., Raadik, T., Kauk-Kuusik, M. & Raudoja, J. Photoluminescence study of disordering in the cation sublattice of Cu_2ZnSnS_4. *Curr. Appl Phys.* **14**, 1424–1427 (2014).
16. Krämmer, C. et al. Reversible order-disorder related band gap changes in $Cu_2ZnSn(S,Se)_4$ via post-annealing of solar cells measured by electroreflectance. *Appl. Phys. Lett.* **105**, 262104 (2014).
17. Yuan, Z. K. et al. Engineering solar cell absorbers by exploring the band alignment and defect disparity: the case of Cu- and Ag-based kesterite compounds. *Adv. Funct. Mater.* **25**, 6733–6743 (2015).
18. Chen, W., Dahliah, D., Rignanese, G.-M. & Hautier, G. Origin of the low conversion efficiency in Cu_2ZnSnS_4 kesterite solar cells: the actual role of cation disorder. *Energy Environ. Sci.* **14**, 3567–3578 (2021).
19. Gershon, T. et al. Photovoltaic materials and devices based on the alloyed kesterite absorber $(Ag_xCu_{1-x})_2ZnSnSe_4$. *Adv. Energy Mater.* **6**, 1502468 (2016).
20. Guchhait, A. et al. Enhancement of open-circuit voltage of solution-processed Cu_2ZnSnS_4 solar cells with 7.2% efficiency by incorporation of silver. *ACS Energy Lett.* **1**, 1256–1261 (2016).
21. Su, Z. et al. Cation substitution of solution-processed Cu_2ZnSnS_4 thin film solar cell with over 9% efficiency. *Adv. Energy Mater.* **5**, 1500682 (2015).
22. Lafond, A. et al. Substitution of Li for Cu in Cu_2ZnSnS_4: toward wide band gap absorbers with low cation disorder for thin film solar cells. *Inorg. Chem.* **56**, 2712–2721 (2017).
23. Su, Z. et al. Device postannealing enabling over 12% efficient solution-processed Cu_2ZnSnS_4 solar cells with Cd^{2+} substitution. *Adv. Mater.* **32**, 2000121 (2020).
24. Li, J., Wang, D., Li, X., Zeng, Y. & Zhang, Y. Cation substitution in earth-abundant kesterite photovoltaic materials. *Adv. Sci.* **5**, 1700744 (2018).
25. Rey, G. et al. Ordering kesterite improves solar cells: a low temperature post-deposition annealing study. *Sol. Energy Mater. Sol. Cells* **151**, 131–138 (2016).
26. Krämmer, C. et al. Order–disorder related band gap changes in $Cu_2ZnSn(S,Se)_4$: impact on solar cell performance. In *Proc. 2015 IEEE 42nd Photovoltaic Specialist Conference (PVSC)* 1–4 (IEEE, 2015).
27. Bourdais, S. et al. Is the Cu/Zn disorder the main culprit for the voltage deficit in kesterite solar cells? *Adv. Energy Mater.* **6**, 1502276 (2016).
28. Zhu, A.-Y., Ding, R.-X., Xu, H.-T., Tong, C.-J. & McKenna, K. P. Cu–Zn cation disorder in kesterite $Cu_2ZnSn(S_xSe_{1-x})_4$ solar cells. *ACS Energy Lett.* **9**, 497–503 (2024).
29. Scragg, J. J. S., Choubrac, L., Lafond, A., Ericson, T. & Platzer-Björkman, C. A low-temperature order–disorder transition in Cu_2ZnSnS_4 thin films. *Appl. Phys. Lett.* **104**, 041911 (2014).
30. Serin, B. & Ellickson, R. T. Determination of diffusion coefficients. *J. Chem. Phys.* **9**, 742–747 (1941).
31. Li, X. H. et al. Atomic ordering kinetics of FePt thin films: nucleation and growth of $L1_0$ ordered domains. *J. Appl. Phys.* **101**, 093911 (2007).
32. Vineyard, G. H. Theory of order–disorder kinetics. *Phys. Rev.* **102**, 981–992 (1956).
33. Maeda, T., Kawabata, A. & Wada, T. First-principles study on alkali-metal effect of Li, Na, and K in Cu_2ZnSnS_4 and $Cu_2ZnSnSe_4$. *Phys. Status Solidi c* **12**, 631–637 (2015).
34. Tajima, S. et al. Sodium distribution in solar-grade Cu_2ZnSnS_4 layers using atom-probe tomographic technique. *Jpn. J. Appl. Phys.* **54**, 112302 (2015).
35. Zhong, G. et al. Induced effects by the substitution of Zn in Cu_2ZnSnX_4 (X = S and Se). *Thin Solid Films* **603**, 224–229 (2016).
36. Maeda, T., Nakamura, S. & Wada, T. First-principles study on Cd doping in Cu_2ZnSnS_4 and $Cu_2ZnSnSe_4$. *Jpn. J. Appl. Phys.* **51**, 10NC11 (2012).
37. Yan, C. et al. Beyond 11% efficient sulfide kesterite $Cu_2Zn_xCd_{1-x}SnS_4$ solar cell: effects of cadmium alloying. *ACS Energy Lett.* **2**, 930–936 (2017).
38. Kuo, D.-H. & Wubet, W. Mg dopant in $Cu_2ZnSnSe_4$: an n-type former and a promoter of electrical mobility up to 120 $cm^2V^{-1}s^{-1}$. *J. Solid State Chem.* **215**, 122–127 (2014).
39. Caballero, R. et al. Effect of magnesium incorporation on solution-processed kesterite solar cells. *Front. Chem.* **6**, 5 (2018).
40. Zhang, L. et al. First-principles study on Mg doping in Cu_2ZnSnS_4. *J. Inorg. Mater.* **35**, 1290–1294 (2020).
41. Dimitrievska, M. et al. Defect characterisation in $Cu_2ZnSnSe_4$ kesterites via resonance Raman spectroscopy and the impact on optoelectronic solar cell properties. *J. Mater. Chem. A* **7**, 13293–13304 (2019).
42. Gürel, T. Characterization of vibrational and mechanical properties of quaternary compounds Cu_2ZnSnS_4 and $Cu_2ZnSnSe_4$ in kesterite and stannite structures. *Phys. Rev. B* **84**, 205201 (2011).
43. Valakh, M. Y. et al. Optically induced structural transformation in disordered kesterite Cu_2ZnSnS_4. *JETP Lett.* **98**, 255–258 (2013).
44. Caballero, R. et al. Non-stoichiometry effect and disorder in Cu_2ZnSnS_4 thin films obtained by flash evaporation: Raman scattering investigation. *Acta Mater.* **65**, 412–417 (2014).
45. Duan, H.-S. et al. The role of sulfur in solution-processed $Cu_2ZnSn(S,Se)_4$ and its effect on defect properties. *Adv. Funct. Mater.* **23**, 1466–1471 (2013).
46. Yu, Z. et al. Unveiling the selenization reaction mechanisms in ambient air-processed highly efficient kesterite solar cells. *Adv. Energy Mater.* **13**, 2300521 (2023).
47. Wu, J. et al. Quantifying the interface defect for the stability origin of perovskite solar cells. *Adv. Energy Mater.* **9**, 1901352 (2019).
48. Kim, S., Márquez, J. A., Unold, T. & Walsh, A. Upper limit to the photovoltaic efficiency of imperfect crystals from first principles. *Energy Environ. Sci.* **13**, 1481–1491 (2020).
49. Shi, J., Li, D., Luo, Y., Wu, H. & Meng, Q. Opto-electro-modulated transient photovoltage and photocurrent system for investigation of charge transport and recombination in solar cells. *Rev. Sci. Instrum.* **87**, 123107 (2016).
50. Shi, J. et al. From ultrafast to ultraslow: charge-carrier dynamics of perovskite solar cells. *Joule* **2**, 879–901 (2018).
51. Li, Y. et al. Exploiting electrical transients to quantify charge loss in solar cells. *Joule* **4**, 472–489 (2020).
52. Peharz, G. et al. Challenges in the industrial production of CZTS monograin solar cells. In *Proc. 2017 IEEE 44th Photovoltaic Specialist Conference (PVSC)* 178–181 (IEEE, 2018).

53. Neubauer, C., Samieipour, A., Oueslati, S., Ernits, K. & Meissner, D. Spatially resolved opto-electrical performance investigations of $Cu_2ZnSnS_{3.2}Se_{0.8}$ photovoltaic devices. *Energy Sci. Eng.* **6**, 563–569 (2018).
54. Clark, S. J. et al. First principles methods using CASTEP. *Z. Kristallogr. Cryst. Mater.* **220**, 567–570 (2005).
55. Perdew, J. P., Burke, K. & Ernzerhof, M. Generalized gradient approximation made simple. *Phys. Rev. Lett.* **77**, 3865 (1996).
56. Govind, N., Petersen, M., Fitzgerald, G., King-Smith, D. & Andzelm, J. A generalized synchronous transit method for transition state location. *Comput. Mater. Sci.* **28**, 250–258 (2003).

Acknowledgements

We acknowledge the Excellent Science and Technology Innovation Group of Jiangsu Province in Nanjing University of Science and Technology for their help in the theoretical calculations and appreciate the valuable help from X. Cheng and Z. Li at Hebei University in the deep level transient spectroscopy measurements. This work was supported by the National Key R&D Program of China (2024YFB4205000 (to J.S.)), National Natural Science Foundation of China (52222212 (to J.S.), 52227803 (to Q.M.), 52172261 (to Y. Luo), 52502322 (to J.W.)), and China National Postdoctoral Program for Innovative Talents (BX20250177 (to J.W.)). J.S. also gratefully acknowledges the support from the Youth Innovation Promotion Association of the Chinese Academy of Sciences (2022006).

Author contributions

J.W., J.S., D.L. and Q.M. conceived the idea and designed the experiments. J.W. and J.S. proposed the theoretical mechanism, and did the experiments and the data analysis. F.M. performed structural measurement and analysis. L.L. and K.Y. participated in improving cell performance and conducting characterization. X.X., M.J. and B.Z. supported CZTSSe solar cell fabrication. Y. Li participated in microstructure and photoelectric characterization. H.W. and Y. Luo supported the discussion. J.W., J.S., D.L. and Q.M. participated in writing the paper.

Competing interests

The authors declare no competing interests.

Additional information

Supplementary information The online version contains supplementary material available at https://doi.org/10.1038/s41560-025-01902-w.

Correspondence and requests for materials should be addressed to Jiangjian Shi, Dongmei Li or Qingbo Meng.

Peer review information *Nature Energy* thanks Simona Olga Binetti and the other, anonymous, reviewer(s) for their contribution to the peer review of this work.

nature portfolio

Corresponding author(s): Qingbo Meng, Dongmei Li, Jiangjian Shi

Solar Cells Reporting Summary

Nature Portfolio wishes to improve the reproducibility of the work that we publish. This form is intended for publication with all accepted papers reporting the characterization of photovoltaic devices and provides structure for consistency and transparency in reporting. Some list items might not apply to an individual manuscript, but all fields must be completed for clarity.

For further information on Nature Research policies, including our data availability policy, see Authors & Referees.

Experimental design

Please check the following details are reported in the manuscript, and provide a brief description or explanation where applicable.

1. Dimensions

Area of the tested solar cells	☒ Yes ☐ No	The area is 0.2694 cm2 and it is given in experimental section and in the certification report. *Explain why this information is not reported/not relevant.*
Method used to determine the device area	☒ Yes ☐ No	The device area is determined by mask and it is given in experimental section and in the certification report. *Explain why this information is not reported/not relevant.*

2. Current-voltage characterization

Current density-voltage (J-V) plots in both forward and backward direction	☒ Yes ☐ No	The forward and backward scan J-V curves are given in certification report and it shows no hysteresis.
Voltage scan conditions	☒ Yes ☐ No	The voltage was forward scanned from -50 mV to 600 mV with a scanning rate of 90 mV·s-1 and it is given in experimental section. *Explain why this information is not reported/not relevant.*
Test environment	☒ Yes ☐ No	The J-V tests were conducted in air at 25 °C. The test environment is given in experimental section. *Explain why this information is not reported/not relevant.*
Protocol for preconditioning of the device before its characterization	☒ Yes ☐ No	No preconditioning of the device was before the measurement. This is given in experimental section. *Explain why this information is not reported/not relevant.*
Stability of the J-V characteristic	☐ Yes ☒ No	*Provide a description of the method used. The stability of the J-V characteristic can be verified with time evolution of the maximum power point or with the photocurrent at maximum power point; see ref. 5 for details.* Kesterite solar cells do not have hysteresis . And in the certification process, maximum power output had been traced for several minutes to confirm the cell efficiency.

3. Hysteresis or any other unusual behaviour

Description of the unusual behaviour observed during the characterization	☐ Yes ☒ No	*Provide a description of hysteresis or any other unusual behaviour observed during the characterization.* Kesterite solar cells do not have hysteresis or other unusual behaviour.
Related experimental data	☐ Yes ☒ No	*Provide a description of the related experimental data.* Kesterite solar cells do not have hysteresis or other unusual behaviour.

4. Efficiency

External quantum efficiency (EQE) or incident photons to current efficiency (IPCE)	☒ Yes ☐ No	Given in supplementary fig. 27. *Explain why this information is not reported/not relevant.*

A comparison between the integrated response under the standard reference spectrum and the response measure under the simulator	☒ Yes ☐ No	The integrated JSC from EQE spectra can support the results of the J–V measurements. *Explain why this information is not reported/not relevant.*
For tandem solar cells, the bias illumination and bias voltage used for each subcell	☐ Yes ☒ No	*Provide a description of the measurement conditions.* No tandem solar cell was studied.

5. Calibration

Light source and reference cell or sensor used for the characterization	☒ Yes ☐ No	The J-V curves of the solar cells were measured by using Keithley Source Meter under simulated AM 1.5 sunlight at 100 mW cm−2 calibrated with Si reference cell. This is given in experimental section. *Explain why this information is not reported/not relevant.*
Confirmation that the reference cell was calibrated and certified	☒ Yes ☐ No	The reference cell was calibrated by National Institute of Metrology, China. This is given in experimental section. *Explain why this information is not reported/not relevant.*
Calculation of spectral mismatch between the reference cell and the devices under test	☒ Yes ☐ No	The mismatch factor is 1.013 and this is given in certification report *Explain why this information is not reported/not relevant.*

6. Mask/aperture

Size of the mask/aperture used during testing	☒ Yes ☐ No	The mask area is 0.2694 cm2 and this is given in certification report *Explain why this information is not reported/not relevant.*
Variation of the measured short-circuit current density with the mask/aperture area	☐ Yes ☒ No	*Report the difference in the short-circuit current density values measured with the mask and aperture area.* No such phenomenon in kesterite solar cells

7. Performance certification

Identity of the independent certification laboratory that confirmed the photovoltaic performance	☒ Yes ☐ No	The photovoltaic performance is certified in NPVM *Explain why this information is not reported/not relevant.*
A copy of any certificate(s)	☒ Yes ☐ No	The certification report is given in supplementary materials *Explain why this information is not reported/not relevant.*

8. Statistics

Number of solar cells tested	☒ Yes ☐ No	18 cells are used for statistic analysis *Explain why this information is not reported/not relevant.*
Statistical analysis of the device performance	☒ Yes ☐ No	Statistical analysis of the device performance is given in figure 5, supplementary figure 1-6 and supplementary figure 10 *Explain why this information is not reported/not relevant.*

9. Long-term stability analysis

Type of analysis, bias conditions and environmental conditions	☐ Yes ☒ No	*Provide a description of the type of analysis, bias conditions and environmental conditions (e.g. illumination type, temperature, atmosphere humidity, encapsulation method, preconditioning temperature, bias) for each long-term stability analysis carried out; see ref. 7 and 8 for details.* No stability problem has been reported in kesterite solar cells